

Electrochemical oxidation of nitric oxide to concentrated nitric acid with carbon-based catalysts at near-ambient conditions

Received: 4 April 2024

Accepted: 26 February 2025

Published online: 3 April 2025



Rong Xia¹, Sydnee Dronsfield², Ahryeon Lee^{1,3}, Bradie S. Crandall^{1,3}, Jiashun Liang⁴, Bjorn Hasa¹, Andy Redder¹, Gang Wu⁴, Tiago J. Goncalves², Samira Siahrostami⁵✉ & Feng Jiao^{1,3}✉

Nitric oxide (NO) emissions pose significant environmental challenges that demand sustainable remediation strategies. Here we report an electrochemical approach to convert NO into salt-free, concentrated nitric acid (HNO₃) using a carbon-based catalyst at near-ambient conditions. The system achieves >90% HNO₃ Faradaic efficiency (FE) at 100 mA cm⁻² with pure NO and retains >70% FE with dilute NO (0.5 vol%). Mechanistic studies identified nitrous acid as a critical intermediate, diverging from conventional thermocatalytic nitrogen dioxide pathways. By implementing a vapour-fed strategy in a membrane electrode assembly electrolyser, we directly synthesized 32 wt% HNO₃ from NO and deionized water, achieving 86% FE at 800 mA cm⁻² without electrolyte additives or downstream purification. This work establishes an electrochemical route to valorize NO emissions to high-purity HNO₃, advancing sustainable pollution mitigation and chemical manufacturing.

Nitric oxide (NO), a key component of NO_x, is a major contributor to environmental issues such as air pollution, acid rain and smog^{1–3}. Chemical plants, metal processing facilities and cement manufacturing operations are the principal sources of NO emissions in the industrial sector^{4–6}. Selective catalytic reduction (SCR) is the most prevalent method for removing NO emissions. However, this process has some limitations as it necessitates operating temperatures in the range of 300–400 °C and consumes additional ammonia as reducing agent. Consequently, SCR demonstrates limited effectiveness at near-ambient temperatures and does not produce any value-added products^{7–9}. An electrochemical process operating at near-ambient temperature is a highly attractive alternative, especially when this process also converts NO waste gas into high-value chemicals such as nitric acid (HNO₃), further enhancing its economic viability for commercial applications¹⁰.

The electrochemical oxidation of NO to HNO₃ presents a promising approach to tackle NO emissions while simultaneously producing valuable HNO₃. Historically, HNO₃ was first synthesized industrially by the Birkeland–Eyde process, in which atmospheric nitrogen was oxidized to NO using plasma arcs at extreme temperatures (>3,000 °C), followed by NO oxidation to HNO₃. While revolutionary for its time, this energy-intensive process was supplanted by the Ostwald process, which relies on ammonia feedstock (from the Haber–Bosch process) and involves the high-temperature catalytic oxidation of NH₃ to produce HNO₃. However, both approaches depend on centralized, capital-intensive facilities and require NO concentrations above 10%, rendering them impractical for low-concentration NO remediation. In contrast, the electrochemical approach can operate at near-ambient temperatures and pressures, enabling modular scalability and

¹Center for Catalytic Science and Technology, Department of Chemical and Biomolecular Engineering, University of Delaware, Newark, DE, USA.

²Department of Chemistry, University of Calgary, Calgary, Alberta, Canada. ³Center for Carbon Management, Department of Energy, Environmental, and Chemical Engineering, McKelvey School of Engineering, Washington University in St Louis, St Louis, MO, USA. ⁴Department of Chemical and Biological Engineering, University at Buffalo, The State University of New York, Buffalo, NY, USA. ⁵Department of Chemistry, Simon Fraser University, Burnaby, British Columbia, Canada. ✉e-mail: ssiahros@sfu.ca; jiaof@wustl.edu

decentralized HNO_3 production close to NO waste sources, thereby reducing transportation costs and emissions. At present, only a few studies on electrochemical NO oxidation have been conducted, and these primarily focused on electrocatalyst development for sensor applications^{11–15}. Furthermore, a concentrated and salt-free HNO_3 product stream is highly desirable to minimize the costs associated with liquid product separation. However, to the best of our knowledge, there are no reports on the electrocatalytic oxidation of NO to HNO_3 with high concentration and purity.

Here we report an electrochemical pathway to convert NO into concentrated HNO_3 using a low-cost carbon-based catalyst. This NO electrooxidation approach achieves >90% Faradaic efficiency (FE) towards HNO_3 . In addition, >70% FE for HNO_3 can be achieved in a dilute NO stream with a concentration of 0.5 vol%. The mechanism of the NO electrooxidation was investigated using online flow electrolyser mass spectrometry (FEMS), isotope-labelling experiments and density functional theory (DFT) calculations. The results suggest that NO is oxidized through a nitrous acid (HNO_2) pathway instead of via a nitrogen dioxide (NO_2) intermediate and hydroxy is the most active oxygen functional group for the electrooxidation of NO to HNO_3 . Finally, we developed a vapour-fed strategy in which NO gas and water vapour were fed into a membrane electrode assembly electrolyser to produce a high-purity, concentrated HNO_3 solution (up to 32 wt%) directly from NO and deionized water at a current density of 800 mA cm^{-2} , without the addition of any electrolyte salts. Energy consumption assessments and techno-economic analysis confirmed that the production of high concentrations of salt-free HNO_3 significantly lowers the cost of its production and is vital for commercial viability. This work demonstrates the production of HNO_3 from NO through an electrochemical process at near-ambient conditions, paving the way for value-added NO remediation strategies.

Results

NO electrooxidation on carbon catalysts

Commercially available activated carbon, namely, Vulcan carbon, was chosen as the model catalyst. The catalyst was characterized by scanning electron microscopy (SEM), Raman spectroscopy and X-ray photoelectron spectroscopy (XPS; Fig. 1a and Supplementary Figs. 1 and 2). The electrochemical NO oxidation reaction was initially conducted in a microfluidic electrolyser paired with the hydrogen evolution reaction. A gas diffusion electrode was used to separate the gas flow chamber from the anolyte, enabling NO electrooxidation to take place at the triple-phase interface. Vulcan carbon and 10 wt% Pt/C served as the anode and cathode, respectively, and 0.05 M H_2SO_4 was used as the electrolyte. This design enabled the direct introduction of the gaseous NO reactant at the electrode surface, bypassing the need for NO dissolution in water (Supplementary Fig. 3). This approach effectively overcomes the mass transport limitations associated with NO in traditional batch-type electrolyzers, which are hampered by the low solubility of NO in aqueous solutions (0.06 g l^{-1} at 25°C)¹⁶. The FE for HNO_3 increased with potential, reaching its peak at 1.73 V versus the reversible hydrogen electrode (RHE) with 92.5% efficiency (Fig. 1b). In contrast, the FE towards HNO_2 exhibited an inverse relationship, decreasing as the potential increased. This observation suggests that higher potentials favour the formation of HNO_3 during NO electrooxidation, whereas lower potentials lead to an increased FE for HNO_2 . At a current density of 200 mA cm^{-2} , an 85.1% FE for HNO_3 production was observed, while the formation of HNO_2 was negligible. For comparison, we fed Ar into the gas chamber instead of NO; as shown in Supplementary Fig. 4, a total current density of 0.8 mA cm^{-2} was observed at 1.8 V versus RHE under Ar atmosphere, indicating poor oxygen evolution activity on Vulcan carbon. A control experiment, in which NO was fed into the electrolyser without an applied potential, showed negligible HNO_3 formation compared with that obtained from electrochemical NO oxidation (Methods and Supplementary Fig. 5). We also conducted isotope-labelling experiments using ^{15}N -labelled NO as the feedstock.

As shown in Supplementary Fig. 6, when ^{15}NO was used instead of ^{14}NO , the resulting HNO_3 showed a clear m/z shift of 1, indicating that NO is the nitrogen source of HNO_3 .

To further understand the electrooxidation of NO, online FEMS was coupled with linear sweep voltammetry (LSV) measurements to reveal the formation of gaseous products during the electrooxidation of NO under 100 vol% NO on carbon catalysts (Fig. 1c,d). FEMS provided high-sensitivity, time-resolved detection at $\sim 100 \mu\text{m}$ from the electrode surface¹⁷. During the LSV scan, the NO signal decreased, indicating that NO was consumed during the electrooxidation process. Concurrently, there was no noticeable change in the carbon dioxide and carbon monoxide signals, indicating that neither carbon monoxide nor carbon dioxide was formed in detectable quantities during the LSV scan. Regarding the liquid products, only HNO_3 and HNO_2 were detected by ion chromatography. No other liquid by-products were observed by ^1H NMR spectroscopy (Supplementary Fig. 7).

We also investigated the electrochemical oxidation of NO at low concentrations (Fig. 1e,f and Supplementary Fig. 8). The experiments revealed FEs for HNO_3 of 80.0% and 71.5% at a current density of 5 mA cm^{-2} with 1 and 0.5 vol% NO, respectively (Fig. 1e,f). We further evaluated the electrochemical NO oxidation reaction using 800 ppm NO (Fig. 1g), comparable to real-world flue gas composition. An 87.5% FE for HNO_3 was achieved at a current density of 1 mA cm^{-2} . While this FE demonstrates potential for dilute NO remediation, the operating current density was significantly below industrial benchmarks. Meanwhile, in a typical flue gas composition, CO_2 , N_2 and O_2 are inert to oxidation and do not interfere with the NO oxidation process, while contaminants such as CO and SO_2 are also amenable to electrochemical oxidation. These findings underscore the potential of electrochemical oxidation for flue gas treatment and the remediation of hazardous emissions. Future work needs to enhance mass transport, catalyst activity and durability at industrially relevant current densities while maintaining selectivity, which is essential for practical deployment.

Reaction mechanism of NO electrooxidation

The reaction mechanism of NO electrooxidation was investigated using online FEMS coupled with isotope-labelling experiments to identify the reaction intermediates and pathways. Three potential reaction pathways were evaluated: oxygen-mediated NO oxidation, NO electrooxidation via NO_2 as a reaction intermediate and NO electrooxidation by the HNO_2 pathway (Fig. 2a). To evaluate the role of the O_2 generated in the water oxidation reaction in the electrooxidation of NO, we conducted additional control experiments using an IrO_2 anode, a well-known oxygen evolution catalyst. Under a 1 vol% NO atmosphere, experiments were conducted at three distinct current densities of 30, 50 and 80 mA cm^{-2} , and the products were monitored by FEMS. With a carbon anode, a substantial decrease in the NO signal was observed on applying a current, indicating that NO was consumed during electrolysis (Fig. 2b). A relatively small increase in the oxygen signal was also observed at higher operating current densities. In contrast, the control experiment with an IrO_2 anode displayed no activity towards NO electrooxidation, but a large increase in the oxygen signal was observed during electrolysis.

Further examination of the FEMS data obtained in conjunction with LSV (Fig. 2c) revealed that the onset potential for the oxygen evolution reaction was $\sim 380 \text{ mV}$ more positive than that of NO electrooxidation on carbon catalysts, suggesting that NO electrooxidation occurs more easily than oxygen evolution on the carbon catalysts. Interestingly, no change in the NO_2 signal was observed throughout the LSV experiment, indicating that there was no significant formation of NO_2 during electrolysis. This observation suggests that the electrooxidation of NO follows a different reaction pathway from the $\text{NO} \rightarrow \text{NO}_2 \rightarrow \text{HNO}_3$ pathway involved in the thermocatalytic oxidation of NO (refs. 18–20). We hypothesize that the NO electrooxidation reaction may follow a HNO_2 pathway in which water serves as the oxygen source rather than O_2 , used in conventional thermocatalytic processes.

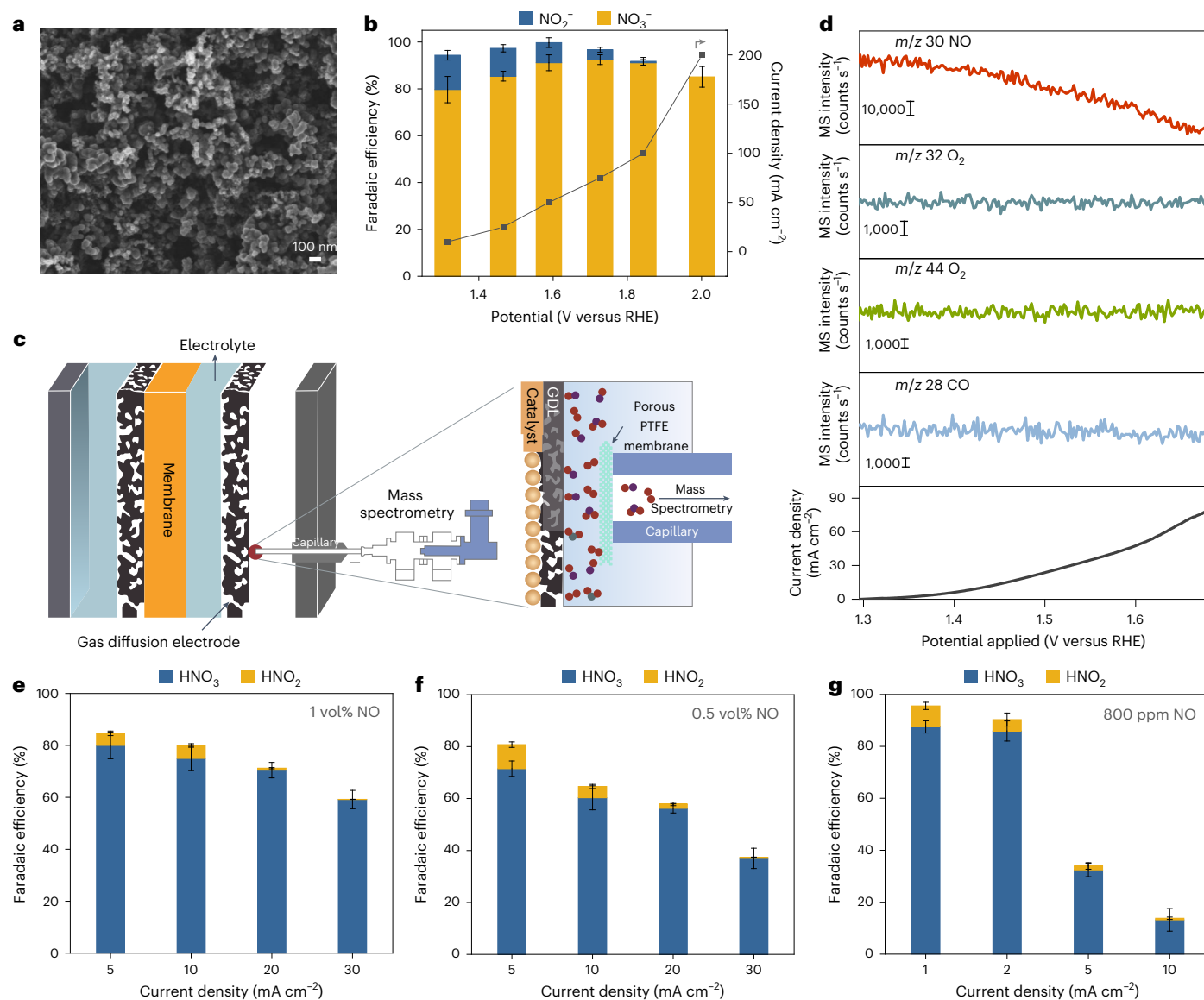


Fig. 1 | Electrooxidation of NO on carbon-based catalysts. **a**, SEM image of the Vulcan carbon used as catalyst for the NO electrooxidation reaction. **b**, Electrochemical NO oxidation on carbon-based catalysts in a three-compartment flow electrolyser coupled with a gas diffusion electrode using 100 vol% NO. **c**, Schematic of online FEMS. A capillary is placed inside the electrolyser at $\sim 100\ \mu\text{m}$ from the electrode surface. GDL, gas diffusion layer; PTFE, polytetrafluoroethylene. **d**, Product detection by FEMS coupled with LSV of NO electrooxidation on carbon-based catalysts in 50 vol% NO. **e–g**, Electrooxidation of NO on carbon-based catalysts under 1 vol% NO (**e**), 0.5 vol% NO (**f**) and 800 ppm NO (**g**) at various applied current densities. Average values were calculated from measurements performed in triplicate; the error bars represent the standard deviation.

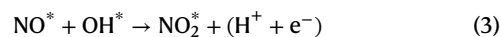
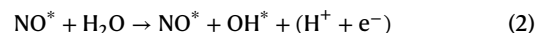
Isotope-labelling experiments confirmed that NO is the nitrogen source of HNO_3 . We also analysed the co-electrolysis of ^{14}NO and H^{15}NO_2 ; the results suggest that 77% of the HNO_3 produced in the co-electrolysis originated from H^{15}NO_2 (Fig. 2d). These findings confirm that HNO_2 can be electrocatalytically converted into HNO_3 ; however, we cannot conclusively prove HNO_2 to be a key intermediate in the electrooxidation of NO based on the isotope-labelling study alone.

DFT calculations

DFT calculations were performed to investigate the mechanism of NO electrooxidation and to identify the active sites on the carbon catalysts. Conventional NO oxidation is considered to follow a $\text{NO} \rightarrow \text{NO}_2$ mechanism, while Anand and co-workers proposed that HNO_2 is involved in the electrooxidation of N_2 to HNO_3 , with NO formed as an intermediate^{18,21–23}. Figure 3a shows two potential mechanisms for this reaction involving either NO_2^* (NO_2^* pathway) or HNO_2^* (HNO_2^*

pathway) as an intermediate. The NO_2^* pathway commences with the adsorption of $\text{NO}(\text{g})$ and the oxidation of a single molecule of H_2O , leading to the formation of NO_2^* as the critical intermediate in the production of HNO_3 . In contrast, the HNO_2^* pathway proceeds via the formation of HNO_2^* as the key intermediate in the formation of HNO_3 . The NO_2^* pathway follows equations (1)–(6), while the HNO_2^* pathway follows equations (7)–(12) (Supplementary Fig. 9).

NO_2^* pathway:



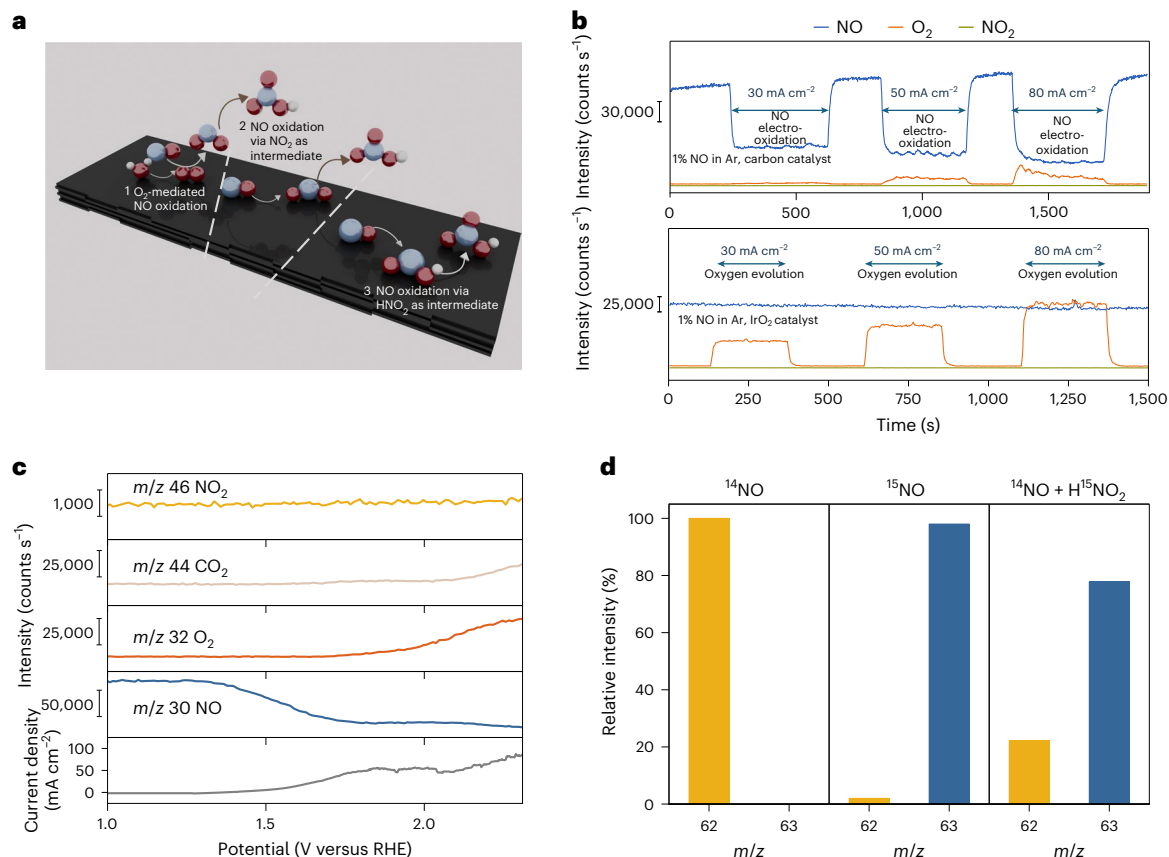
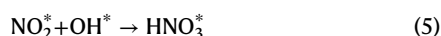
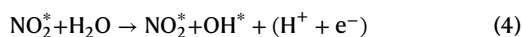
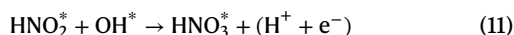
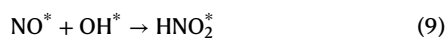
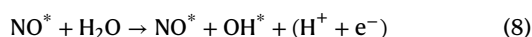


Fig. 2 | Reaction mechanism of NO electrooxidation on carbon-based catalysts. **a**, Possible reaction mechanism of NO electrooxidation: O₂-mediated NO oxidation (1), NO electrooxidation via NO₂ as reaction intermediate (2) and NO electrooxidation via HNO₂ as reaction intermediate (3). **b**, Investigation of the role of O₂ evolution in NO electrooxidation. Vulcan carbon and IrO₂ were used as catalysts. IrO₂ is inert towards NO oxidation and selectively produces

O₂ under a 1 vol% NO atmosphere. **c**, Determination of the onset potentials of NO electrooxidation, oxygen evolution, and CO₂ and NO₂ formation under a 1 vol% NO atmosphere using online FEMS coupled with LSV. **d**, Isotope-labelling electrochemical NO oxidation experiments, performed by feeding ¹⁴NO, ¹⁵NO and a mixture of ¹⁴NO and H¹⁵NO₂ into the electrolyser.



HNO₂* pathway:



In the present study, Vulcan carbon was used as the model catalyst for the electrooxidation of NO to HNO₃. XPS analysis confirmed the

presence of oxygen-containing functional groups on the Vulcan carbon surface, consistent with the literature²⁴. To elucidate the active sites for NO electrooxidation, we simulated various oxygen-containing functional groups, namely, hydroxy (OH), carbonyl (CO), carboxy (COOH) and quinone (COCO) groups, on the zigzag and armchair edges of the carbon catalyst (Fig. 3b). Note that pristine graphene, which does not bind reaction intermediates, has been demonstrated to be inert towards electrochemical reactions such as the oxygen reduction and oxygen evolution reactions²⁵. The above model structures have been extensively studied as representative models of carbon structures containing edge oxygen functional groups^{26,27}. They have demonstrated involvement in various electrochemical reactions, such as the oxygen reduction reaction (ORR) to hydrogen peroxide. The *sp*²-carbon atoms of zigzag edges fully covered with hydroxy and carbonyl groups have been observed to exhibit strong and weak active sites for the ORR, respectively. Incorporating carboxy and quinone groups onto hydrogen-truncated *sp*²-carbon atoms has been shown to enhance the ORR^{26,27}. This modification specifically enables the influence of carboxy and quinone groups on catalytic mechanisms to be investigated, which is crucial to understand the mechanism involved in NO oxidation. We examined various active sites close to the oxygen functional groups in each model structure and identified the carbon atom adjacent to the oxygen functional group as the most active site. In addition, various adsorbate orientations were considered and the most energetically stable one was chosen for our analysis.

DFT calculations were conducted to determine the most probable pathway for NO electrooxidation with the consideration of all possible

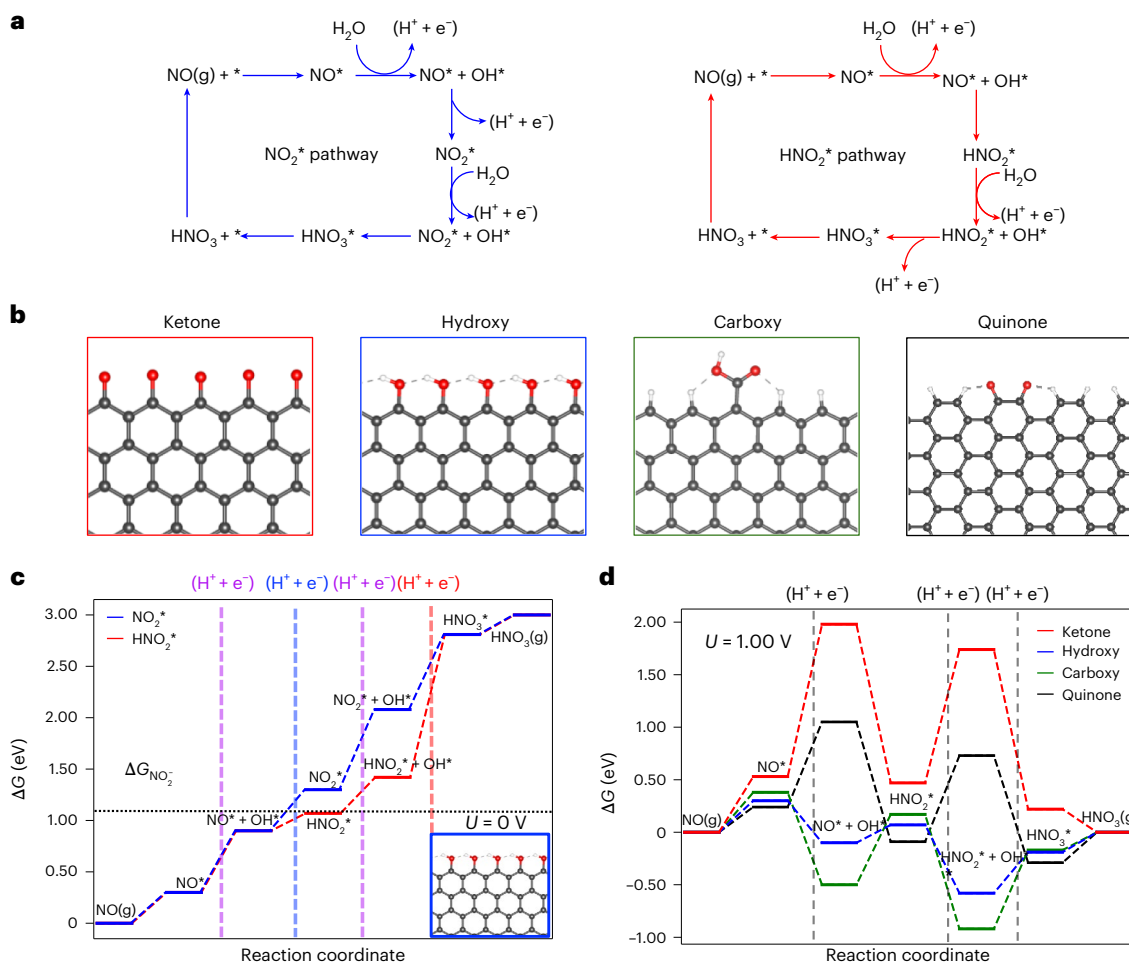


Fig. 3 | DFT analysis of the reaction mechanism. **a**, Possible reaction mechanisms for electrochemical NO oxidation to HNO₃. **b**, Optimized structures of four oxygen functional groups on graphene edge sites. The structures show carbonyl, hydroxy and carboxy groups on the zigzag edges and quinone on the armchair edges of the carbon catalyst. **c**, Free-energy diagrams of electrochemical NO oxidation on hydroxy edge structures at an applied potential of 0 V, comparing the NO₂* and HNO₂* pathways. The purple dashed lines show

the electrochemical steps that both the NO₂* and HNO₂* pathways share, the blue dashed line indicates the electrochemical steps specific to the NO₂* pathway and the red dashed line highlights the electrochemical step specific to the HNO₂* pathway. The horizontal black dotted line at -1.20 eV represents the free energy of NO₂⁻ formation. **d**, Free-energy diagrams of the electrooxidation of NO on ketone, hydroxy, carboxy and quinone functional groups at an applied potential of 1.00 V. The grey dashed lines showcase the electrochemical steps.

intermediates along the reaction path. Figure 3c shows the free-energy diagrams calculated for both the NO₂* and HNO₂* mechanisms using the hydroxy zigzag model structure. The free-energy diagrams reveal that the HNO₂* intermediate is energetically more favourable than NO₂*, suggesting a preference for the HNO₂* pathway over the NO₂* pathway on the hydroxy zigzag edge. The free-energy diagrams for the other three structures are presented in Supplementary Fig. 10, which reveal similar behaviour, signifying a general inclination towards the HNO₂* pathway over the NO₂* pathway for Vulcan carbon. The horizontal black dotted line in Fig. 3c shows the free energy of NO₂⁻ formation for an applied potential U of 0 V (Supplementary Note 1). The free energy of NO₂* is close to the reference line for several of the surfaces that we examined. This suggests a tendency for NO₂* to desorb into solution as NO₂⁻ when the applied potential is $U = 0$ V. However, at an applied potential of 1.00 V, which falls within the oxidation range (indicating a positive charge on the electrode), we expect that NO₂⁻, if formed, will return to the surface. This behaviour is likely to facilitate further oxidation, leading to the formation of HNO₃. This prediction is grounded in the typical behaviour of NO₂⁻ under electrochemical conditions and underscores the dynamic nature of its interaction with the electrode surface.

To identify the activity trend across different oxygen functional groups, we mapped the free-energy diagrams for all four examined

structures at the NO electrooxidation standard redox potential ($U = 1.00$ V) following the HNO₂* pathway (Fig. 3d). Comparison of the free-energy diagrams for the electrooxidation of NO at 0 and 1.00 V on all four studied surfaces (Supplementary Fig. 11) revealed that the hydroxy zigzag edge exhibits the highest activity for NO electrooxidation to HNO₃ and that the carboxy zigzag edge is the second most active structure. Ketone and quinone require a higher overpotential to overcome the initial electrochemical oxidation step, which would impede their catalytic performance as active sites. While the carboxy functional group edge demonstrates a more thermodynamically favourable first oxidation step, its activity is constrained by the desorption of HNO₃* to form HNO₃(aq). This analysis suggests that NO electrooxidation occurs by the HNO₂* pathway and that hydroxy is the most active oxygen functional group for the electrochemical conversion of NO to HNO₃. We note that identifying a transition state is essential in chemical steps such as the reaction of NO* + OH* to form HNO₂*. To determine the significance of this transition state, we conducted calculations to assess the transition-state energy for the formation of HNO₂* from NO* + OH* on the carboxy zigzag edge. Nudged elastic band (NEB) calculations were performed to investigate the transition state and the associated energy barriers for the reaction NO* + OH* → HNO₂* (Supplementary Fig. 12). These calculations indicated that the transition-state energy

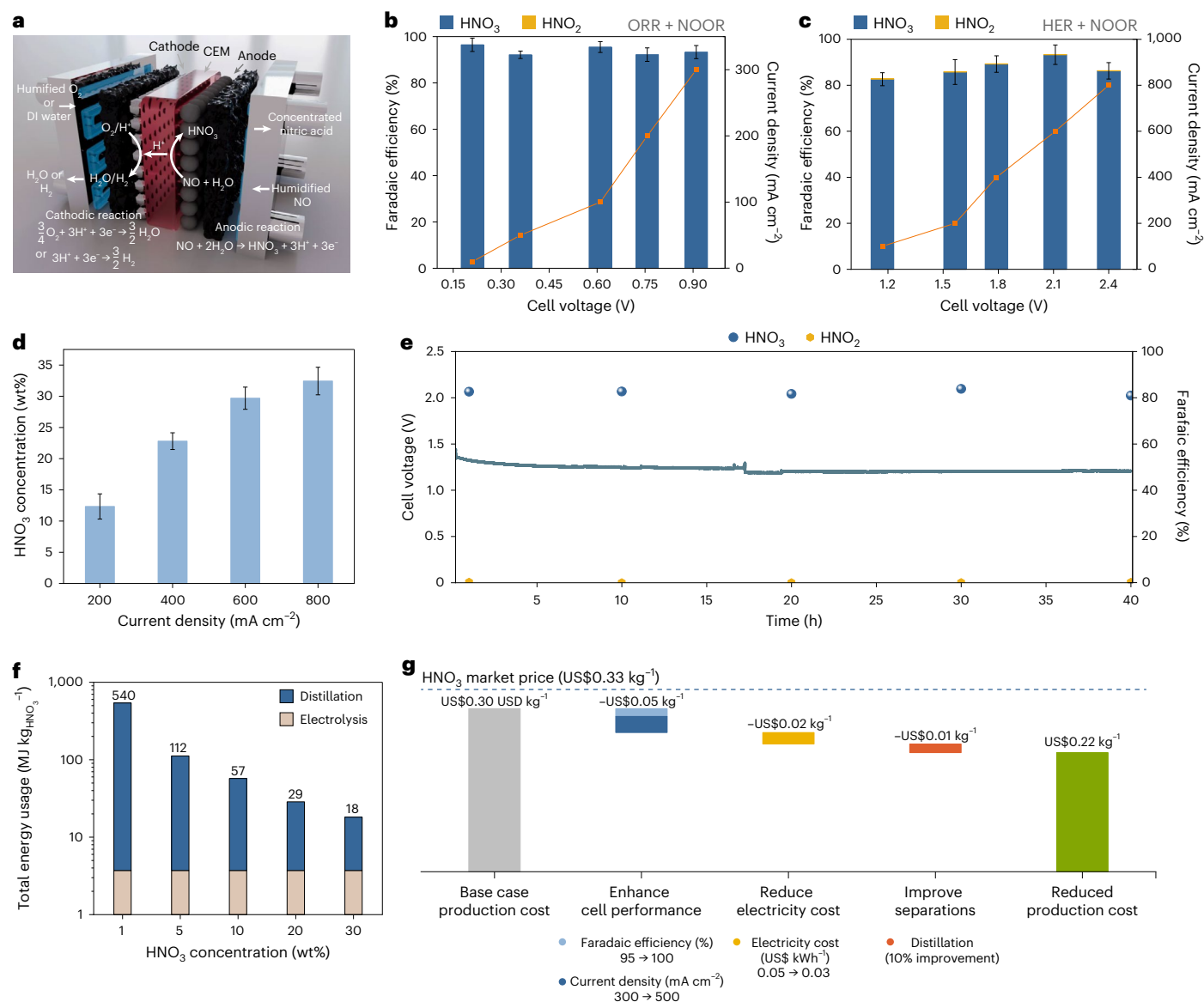


Fig. 4 | Production of salt-free, concentrated HNO₃ directly from NO and deionized water. a, Schematic of a membrane electrode assembly-based zero-gap electrolyser for electrochemical NO oxidation paired with the ORR or HER. NO and water vapour are fed into the anodic chamber and concentrated HNO₃ is condensed by a cold trap at the outlet. DI, deionized; CEM, cation exchange membrane. **b**, NO electrooxidation paired with the ORR in 100 vol% NO, leveraging an iron single-atom Fe-N-C catalyst as the cathode and a carbon-based catalyst as the anode. NOOR, nitric oxide oxidation reaction. **c**, NO electrooxidation coupled with the HER in 100 vol% NO, with Pt/C as the

cathode and a carbon-based catalyst as the anode. **d**, Concentration of HNO₃ produced directly from the NO electrolyser at various current densities using 100 vol% NO. **e**, Stability test at 100 mA cm⁻² over a span of 40 h in 100 vol% NO. **f**, Impact of product concentration on total energy usage, including electrolyser operation at 300 mA cm⁻² and effluent distillation to 68 wt% HNO₃. **g**, Roadmap for electrochemical HNO₃ production. Average values were calculated from measurements performed in triplicate; the error bars represent the standard deviation.

for this step is 0.35 eV, which is typically regarded as surmountable at room temperature (~298 K). At this temperature, the available thermal energy is sufficient for molecules to overcome the energy barrier. We would like to emphasize that while our DFT calculations are consistent with the experimental results, some level of uncertainty remains in the model due to the inherent complexities of the reaction mechanisms. We acknowledge that not all aspects can be fully resolved, and that some degree of speculation is unavoidable. For example, we did not account for the effects of solvent and pH in this study as our focus was on establishing mechanistic insights using DFT calculations in a vacuum. Accurately modelling solvent effects requires explicit solvent models, which is beyond the scope of this study. However, to enhance accuracy, we included a 0.3 eV solvent correction for steps involving

OH* species in all our free-energy diagrams, as suggested in the literature²⁸. In addition, we did not apply pH corrections to our free-energy diagrams. The pH in our experiments can vary with the operating current density, ranging from 0.75 to ~0.6, which would introduce a constant minor shift in the free energy. As illustrated in the example in Supplementary Fig. 13, this shift does not affect the conclusions of our work.

Salt-free HNO₃ production in a zero-gap electrolyser

In conventional batch-type or three-compartment flow electrolyzers, HNO₃ produced by NO electrooxidation often ends up as a diluted stream mixed with a supporting electrolyte, such as potassium hydroxide or sulfuric acid (H₂SO₄). This necessitates energy-intensive

downstream separation processes. To produce a concentrated HNO_3 stream free of any supporting electrolyte, we developed a vapour-feed strategy in which NO gas and water vapour are fed into a membrane electrode assembly-based zero-gap electrolyser (Fig. 4a). The concentrated HNO_3 product is condensed and collected using a cold trap at the outlet of the anodic chamber. The need for electrolyte salts is eliminated by using an ion exchange membrane as the solid electrolyte and only NO and deionized water are fed into the system (Methods).

When NO electrooxidation was coupled with the ORR, leveraging an iron single-atom Fe–N–C catalyst at the cathode, the whole electrolysis process required a full cell voltage of only 0.6 V at a current density of 100 mA cm^{-2} , achieving a 95.5% FE for HNO_3 (Fig. 4b). When paired with the hydrogen evolution reaction (HER), the electrolyser not only converted NO into HNO_3 but also produced valuable H_2 . A full cell voltage of 2.1 V was required to achieve 600 mA cm^{-2} and a 93.3% FE for HNO_3 (Fig. 4c). The equilibrium potential of each reaction is provided in Supplementary Note 2. The corresponding rates of production of HNO_3 are shown in Supplementary Fig. 14. In addition, we successfully achieved a 32 wt% HNO_3 stream directly from the NO electrolyser operated at 800 mA cm^{-2} (Fig. 4d). The stability of the process was demonstrated by continuous electrolysis for 40 h at a constant current density of 100 mA cm^{-2} , with the full cell voltage decreasing from 1.38 V to 1.2 V and the FE for HNO_3 remaining above 80% (Fig. 4e). The post-reaction carbon electrode was characterized by SEM, Raman spectroscopy and XPS. The SEM analysis showed that the morphology of the carbon catalyst remained largely unchanged after 40 h (Supplementary Fig. 15). Raman spectroscopy showed a slight increase in the D/G intensity ratio from 2.5 to 2.8, implying an increase in defect sites on the carbon skeleton (Supplementary Fig. 16). XPS showed that the total oxygen content on the carbon surface increased from 4.1% to 12.1% (Supplementary Figs. 17 and 18), suggesting the formation of oxygen-containing functional groups on the carbon catalyst surface; deconvolution of the C 1s XPS spectra revealed a slight increase in the ratio of carbonyl functional groups (Supplementary Fig. 18). In addition, cyclic voltammetry measurements indicated an increase in the double-layer capacitance after electrolysis (Supplementary Fig. 19), further confirming the formation of oxygen-containing functional groups on the carbon surface²⁹. While these post-reaction characterizations showed clear evidence of surface oxidation of the carbon catalyst after electrolysis for 40 h, the oxidation did not affect the catalytic properties of the carbon catalyst in any substantial way.

To illustrate the cost benefit for producing concentrated salt-free HNO_3 , we analysed the energy consumption associated with electrolysis and distillation across various HNO_3 concentrations (Fig. 4f). The results indicate that at lower HNO_3 concentration, the distillation energy can reach as high as $536.6 \text{ MJ per kg HNO}_3$. Salt removal will further increase energy consumption, making the whole process economically uncompetitive. However, producing HNO_3 with a concentration above 20 wt% directly at the electrolyser outlet minimizes distillation costs, which is a key factor for commercial feasibility. The economic viability of the base case process demonstrated in this work was evaluated via techno-economic modelling, revealing a production cost of HNO_3 of $\text{US\$}0.30 \text{ kg}^{-1}$ (Fig. 4g). A breakdown of the current production cost for electrochemical HNO_3 was used to inform a roadmap for future improvement in commercial viability. By enhancing cell performance, reducing the price of renewable electricity and producing more concentrated HNO_3 , it is possible to achieve a production cost of HNO_3 of $\text{US\$}0.22 \text{ kg}^{-1}$.

The electrochemical oxidation of NO offers substantial potential for reducing industrial NO emissions, particularly in sectors with significant NO emissions and high HNO_3 demand. For example, metal mining operations, which generate significant NO emissions and consume substantial amounts of HNO_3 , could greatly mitigate environmental impacts by converting emitted NO into valuable HNO_3 on-site through electrochemical NO oxidation. In addition, the Ostwald

process, another notable source of NO emissions, is commonly integrated with the Haber–Bosch process. Electrochemical NO oxidation could be integrated with hydrogen evolution in a single electrolyser, supplying green hydrogen to the Haber–Bosch process and converting NO emissions from the Ostwald process to HNO_3 (Supplementary Fig. 22). Electrochemical NO oxidation could also be coupled with ammonia oxidation in a solid electrolyte fuel cell, which concurrently produces NO from ammonia and generates electricity³⁰. Ideally, this electricity could be used to power the electrochemical NO oxidation process, enabling a tandem reaction that converts NH_3 to HNO_3 .

Conclusions

We have demonstrated an electrochemical approach for converting NO into salt-free concentrated HNO_3 employing a carbon-based catalyst. Using a gas diffusion electrode and membrane electrode assembly electrolyser, we have achieved >90% FE in HNO_3 production and generated a 32 wt% HNO_3 product stream at a current density of 800 mA cm^{-2} . Our mechanistic investigations revealed that the NO electrooxidation reaction proceeds through a HNO_2 pathway on a carbon catalyst. A techno-economic assessment and energy consumption analysis demonstrated the economic feasibility of the state-of-the-art NO electrooxidation to HNO_3 reported here. This work sets the stage for the advancement of value-added NO remediation strategies, fostering more sustainable, cost-effective HNO_3 production and contributing to environmental protection efforts.

Methods

Electrode preparation

Vulcan carbon (Fuel Cell Store) was used as the catalyst for NO electrooxidation. The gas diffusion electrode was typically fabricated as follows: 100 mg Vulcan carbon was added to 10 ml isopropanol and 100 μl Nafion ionomer (10 wt%, Fuel Cell Store) to prepare a catalyst ink. The catalyst ink was sonicated for 30 min and then spray-coated onto a gas diffusion layer (Sigracet 39BB, Fuel Cell Store) with a loading of 0.5 mg cm^{-2} . Pt/C (10 wt% Pt mass fraction of the whole catalyst, Fuel Cell Store) was used as the cathodic catalyst for the HER. The Pt/C catalyst was sprayed onto carbon paper with a loading of 0.5 mg cm^{-2} , corresponding to a platinum loading of 0.05 mg cm^{-2} . Iridium oxide (99.9%, Sigma-Aldrich) was used as the oxygen evolution reaction catalyst in control experiments.

Synthesis of the Fe–N–C catalyst

The Fe–N–C catalyst was derived from Fe_2O_3 -doped zeolitic imidazolate framework 8 (ZIF-8) according to the literature³¹. Typically, the Fe_2O_3 -doped ZIF-8 was prepared by pouring a solution of 7.88 g 2-methylimidazole in 150 ml methanol into a solution of 10 mg Fe_2O_3 ($\sim 5 \text{ nm}$, Alfa Aesar) and 6.78 g $\text{Zn}(\text{NO}_3)_2$ in 150 ml methanol at room temperature, followed by stirring for 20 min. The mixture was kept at 60°C for 24 h. The resulting Fe_2O_3 -doped ZIF-8 was collected by centrifugation and washed with ethanol three times. The resulting Fe_2O_3 -doped ZIF-8 powder was dried in a vacuum oven at 60°C for 12 h. The Fe–N–C catalyst was obtained by pyrolysing 300 mg Fe_2O_3 -doped ZIF-8 powder in forming gas (10% H_2/Ar) at $1,100^\circ\text{C}$ for 1 h.

NO electrooxidation in a three-compartment flow electrolyser

NO electrooxidation was first conducted in a three-compartment flow electrolyser coupled with a gas diffusion electrode. The active area of the electrode was 1 cm^2 . A Nafion 212 membrane (Fuel Cell Store) was used to separate the cathodic and anodic chambers. A gas diffusion electrode was used to separate the gas flow chamber from the anolyte, enabling the NO electrooxidation to take place at the triple-phase interface. Vulcan carbon and 10 wt% Pt/C served as the anode and cathode, respectively, and 1 M sodium hydroxide was used as the electrolyte. A Ag/AgCl electrode (Pine Research) was used as the reference electrode. The flow rate of the catholyte and anolyte was controlled by peristaltic

pumps at 0.7 ml min^{-1} . Two types of NO cylinder were used in the experiment: 5 vol% NO (99.9% purity) and 100 vol% NO (99.5% purity), both purchased from Praxair. The concentrations of 0.5, 1 and 2 vol% refer to volume per cent compositions, diluted from 5 vol% NO gas and balanced with argon. Control experiments were performed by feeding NO into the electrolyser for durations equivalent to those used in the electrochemical NO oxidation experiments; this procedure was repeated three times before each electrochemical NO oxidation experiment. The average HNO_3 levels measured in these control experiments were considered as background HNO_3 concentrations and were subsequently subtracted from all data reported in this study. The HNO_3 detected in the control experiments was negligible compared with the HNO_3 produced in the electrochemical oxidation reactions (Supplementary Fig. 5). Chronopotentiometry and LSV of the NO electrooxidation experiments were conducted using a potentiostat (Autolab PG128N, Metrohm). Liquid products (nitrate and nitrite) were quantified by ionic chromatography (Metrohm IC Pro) using a $3.2 \text{ mM Na}_2\text{CO}_3 + 1 \text{ mM NaHCO}_3$ solution as eluent. The methods used for product quantification are described in detail in Supplementary Note 3. The rates of production of HNO_3 and HNO_2 are reported in Supplementary Figs. 8 and 14.

NO electrooxidation in a membrane electrode assembly electrolyser

Titanium endplates were used for both the cathodic and anodic chambers. A membrane electrode assembly was constructed by hot pressing the catalyst coated on carbon cloth onto the activated Nafion 115 membrane with an active area of 5 cm^2 . When NO electrooxidation was paired with the HER, 10 wt% Pt/C (Fuel Cell Store) was used as the cathode and Vulcan carbon was used as the anode. Deionized water was fed into the cathodic chamber without any supporting electrolyte and NO was fed with water vapour to the anode. When coupled with the ORR, an Fe–N–C catalyst was used as the cathode and fed with humidified oxygen. NO was bubbled through a humidifier before being fed to the anode. The feed rate of water vapour was finely tuned through the humidifier temperature and gas flow rate, ensuring that it aligned with the rate of HNO_3 production. To avoid water vapour condensation and flooding of the catalyst layer, the electrolyser was operated at an elevated temperature, ensuring that the relative humidity stayed below 80%. In this study, the humidifier was operated at 45°C , while the electrolyser was maintained at 70°C and the intermediary gas line was kept at 75°C . These conditions facilitated the efficient removal of HNO_3 , with post-electrolysis deionized water flushing accounting for less than 1% of the total HNO_3 produced. To collect concentrated HNO_3 , an ice trap was added to the outlet of the anodic chamber, where HNO_3 carried by the water vapour condensed as concentrated HNO_3 .

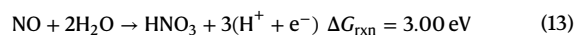
FEMS spectrometry

FEMS was used to identify the gaseous and volatile products formed during the NO electrooxidation reaction, as reported in our previous paper¹⁷. In short, a polyether ether ketone capillary (McMaster, inner diameter 0.25 mm) enclosed by a hydrophobic PTFE membrane (TISCH, pore size $200 \mu\text{m}$) was inserted into the electrolyser at $\sim 100 \mu\text{m}$ from the electrode surface, which allowed only volatile and gaseous products to enter the vacuum chamber, stopping the aqueous electrolyte. Differential pumps (DUO 20 M, Pfeiffer), and a mass spectrometer (Hidden Quadrupole) were used for the analysis. Product samples were ionized at a potential of 70 eV using a 1,700 V secondary electron detection voltage and a $200 \mu\text{A}$ emission current.

DFT calculations

DFT calculations were performed using the Vienna Ab initio Simulation Package (VASP)^{32–34}. The Bayesian error estimation functional with van der Waals (BEEF–vdW) exchange–correlation functional was used with a convergence energy cut-off of 500 eV per atom³⁵. To model the graphene edge, the nanoribbon model structure was adapted

in the Atomic Simulation Environment (ASE) package³⁵. Both zigzag and armchair edge sites were studied, with an 18-Å vacuum layer in both the x and y directions. Unit cell sizes of 4×5 were used. Monkhorst–Pack k -points were sampled using a $1 \times 4 \times 1$ grid, which is the optimum value for ribbon structures²⁶. For structural relaxation, the atom positions of the adsorbates and carbon atoms in graphene were optimized until the forces on each atom were less than 0.01 eV \AA^{-1} and the total energy change was below 10^{-7} eV . The ionic positions were optimized using the quasi-Newton algorithm, implemented in VASP with the ionic relaxation mode (IBRION) parameter set to 2. During the DFT optimization, various configurations were considered for the interaction of each adsorbate with the active sites, and the most stable ones were selected to construct the free-energy diagrams^{18,26,36}. The free energy of each intermediate was calculated using the free energy of HNO_3 as a reference. A correction of 1.12 eV was applied to each step to compensate for the DFT error in estimating the HNO_3 formation energy, as recommended in ref. 37. The Gibbs free energy of adsorption (ΔG) was calculated from $\Delta G = \Delta E_{\text{DFT}} + \Delta(\text{ZPE} - TS)$, where ΔE_{DFT} is the electronic energy change obtained from DFT calculations, ZPE is the zero-point energy, T is the temperature and S is the entropy. ZPE and TS were calculated using the harmonic oscillator implementations within the ASE package. The final ΔG for each step was calculated with respect to $\text{HNO}_3(\text{g})$, $\text{NO}(\text{g})$, $\text{H}_2\text{O}(\text{g})$ and $\text{H}_2(\text{g})$:



where ΔG_{rxn} is the reaction free energy. Use of the BEEF–vdW functional yielded $\Delta G_{\text{rxn}} = 2.37 \text{ eV}$, indicating a correction of 0.63 eV should be applied. Details of the corrections used in the calculations are provided in Supplementary Note 4.

NEB calculations were performed to investigate the transition state and energy barriers associated with $\text{NO}^* + \text{OH}^* \rightarrow \text{HNO}_2$ using VASP³⁸, employing DFT with the BEEF–VdW functional³⁹ for the exchange–correlation energy. Before the NEB calculations, the initial and final configurations of the reaction pathway were optimized. A total of seven images were generated to represent the reaction pathway, including both the initial and final states. To accurately locate the transition state, the climbing image NEB method was employed, allowing the highest energy image to move along the reaction coordinate. Force convergence criteria were set to ensure that the forces acting on the images converged to within 0.01 eV \AA^{-1} . For Brillouin zone sampling, a Monkhorst–Pack grid of $(1 \times 4 \times 1)$ was used, ensuring accurate representation of the electronic structure. The plane-wave energy cut-off was established at 500 eV to achieve sufficient computational accuracy. Following the NEB calculations, the resulting potential energy surface was analysed to extract activation energies and geometries of the transition states.

Techno-economic analysis

The techno-economic simulation of the electrolyser system was based on our previously published custom model^{40,41}. This electrolyser model was adjusted to account for the ORR at the cathode and NO oxidation at the anode using the experimental data presented in this work. The cost of the carbon catalyst materials associated with the cathodic and anodic reactions were also taken into account (Supplementary Note 5). The electrolyser stack was modelled at a production scale of 10,000 kg HNO_3 per day to simulate the scale of a typical industrial HNO_3 plant⁴². The electrochemical production cost of HNO_3 was assessed by performing a numerical evaluation of the price of HNO_3 needed to achieve a net present value of zero at the end of a 20-year plant life. Separation was modelled to further concentrate the HNO_3 to 68 wt%, the concentration at which most HNO_3 is sold⁴³. The separation portion of the techno-economic simulation was performed in the ASPEN Plus software using the economic and energy analyser plugins and a RadFrac distillation column. Additional details of the separation modelling are provided in Supplementary Note 6.

Data availability

The data supporting the findings of this study are included within the article and its Supplementary Information. All other data supporting the findings of the study are available from the corresponding authors upon reasonable request. Source data are provided with this paper.

References

1. Srivastava, R. K. et al. Controlling NO_x emission from industrial sources. *Environ. Prog.* **24**, 181–197 (2005).
2. Kim, S.-W. et al. Satellite-observed U.S. power plant NO_x emission reductions and their impact on air quality. *Geophys. Res. Lett.* **33**, L22812 (2006).
3. Shaw, S. & Van Heyst, B. Nitrogen oxide (NO_x) emissions as an indicator for sustainability. *Environ. Sustain. Indic.* **15**, 100188 (2022).
4. Kasper, J. M., Clausen, C. A. III & Cooper, C. D. Control of nitrogen oxide emissions by hydrogen peroxide-enhanced gas-phase oxidation of nitric oxide. *J. Air Waste Manage. Assoc.* **46**, 127–133 (1996).
5. Luck, F. & Roiron, J. Selective catalytic reduction of NO_x emitted by nitric acid plants. *Catal. Today* **4**, 205–218 (1989).
6. Saramok, M. et al. Modified zeolite catalyst for a NO_x selective catalytic reduction process in nitric acid plants. *Catalysts* **11**, 450 (2021).
7. Forzatti, P. Present status and perspectives in de-NO_x SCR catalysis. *Appl. Catal. A* **222**, 221–236 (2001).
8. Han, L. et al. Selective catalytic reduction of NO_x with NH₃ by using novel catalysts: state of the art and future prospects. *Chem. Rev.* **119**, 10916–10976 (2019).
9. Busca, G., Lietti, L., Ramis, G. & Berti, F. Chemical and mechanistic aspects of the selective catalytic reduction of NO_x by ammonia over oxide catalysts: a review. *Appl. Catal. B* **18**, 1–36 (1998).
10. Ko, B. H., Hasa, B., Shin, H., Zhao, Y. & Jiao, F. Electrochemical reduction of gaseous nitrogen oxides on transition metals at ambient conditions. *J. Am. Chem. Soc.* **144**, 1258–1266 (2022).
11. Ho, K.-C., Hung, W.-T. & Yang, J.-C. On the electrooxidation and amperometric detection of NO gas at the Pt/Nafion® electrode. *Sensors* **3**, 290–303 (2003).
12. Ho, K.-C., Liao, J.-Y. & Yang, C.-C. A kinetic study for electrooxidation of NO gas at a Pt/membrane electrode—application to amperometric NO sensor. *Sens. Actuators B* **108**, 820–827 (2005).
13. Xu, X., Yang, L., Jiang, S., Hu, Z. & Liu, S. High reaction activity of nitrogen-doped carbon nanotubes toward the electrooxidation of nitric oxide. *Chem. Commun.* **47**, 7137–7139 (2011).
14. Kan, K. et al. Amidation of single-walled carbon nanotubes by a hydrothermal process for the electrooxidation of nitric oxide. *Nanotechnology* **20**, 185502 (2009).
15. Maluta, J. R., Canevari, T. C. & Machado, S. A. S. Sensitive determination of nitric oxide using an electrochemical sensor based on MWCNTs decorated with spherical Au nanoparticles. *J. Solid State Electrochem.* **18**, 2497–2504 (2014).
16. Zacharia, I. G. & Deen, W. M. Diffusivity and solubility of nitric oxide in water and saline. *Ann. Biomed. Eng.* **33**, 214–222 (2005).
17. Hasa, B., Jouny, M., Ko, B. H., Xu, B. & Jiao, F. Flow electrolyzer mass spectrometry with a gas-diffusion electrode design. *Angew. Chem. Int. Ed.* **60**, 3277–3282 (2021).
18. Jin, J. et al. Insight into room-temperature catalytic oxidation of nitric oxide by Cr₂O₃: a DFT study. *ACS Catal.* **8**, 5415–5424 (2018).
19. Wang, Z., Lv, G., Zhang, C. & Sun, X. Catalytic oxidation mechanism of NO to HNO₃ on TiO₂ (101) and (001) surfaces and the influence factors on NO removal: a DFT study. *J. Environ. Chem. Eng.* **9**, 104643 (2021).
20. Ma, L. et al. Catalytic performance and reaction mechanism of NO oxidation over Co₃O₄ catalysts. *Appl. Catal. B* **267**, 118371 (2020).
21. Chen, Z., Liu, X., Cho, K., Chen, R. & Shan, B. Density functional theory study of the oxygen chemistry and NO oxidation mechanism on low-index surfaces of SmMn₂O₅ mullite. *ACS Catal.* **5**, 4913–4926 (2015).
22. Anand, M., Abraham, C. S. & Nørskov, J. K. Electrochemical oxidation of molecular nitrogen to nitric acid—towards a molecular level understanding of the challenges. *Chem. Sci.* **12**, 6442–6448 (2021).
23. Dai, C., Sun, Y., Chen, G., Fisher, A. C. & Xu, Z. J. Electrochemical oxidation of nitrogen towards direct nitrate production on spinel oxides. *Angew. Chem. Int. Ed.* **59**, 9418–9422 (2020).
24. Kim, S. et al. Room-temperature metastability of multilayer graphene oxide films. *Nat. Mater.* **11**, 544–549 (2012).
25. Liao, L., Peng, H. & Liu, Z. Chemistry makes graphene beyond graphene. *J. Am. Chem. Soc.* **136**, 12194–12200 (2014).
26. Lu, Z. et al. High-efficiency oxygen reduction to hydrogen peroxide catalysed by oxidized carbon materials. *Nat. Catal.* **1**, 156–162 (2018).
27. Han, G.-F. et al. Building and identifying highly active oxygenated groups in carbon materials for oxygen reduction to H₂O₂. *Nat. Commun.* **11**, 2209 (2020).
28. Heenen, H. H., Gauthier, J. A., Kristoffersen, H. H., Ludwig, T. & Chan, K. Solvation at metal/water interfaces: an ab initio molecular dynamics benchmark of common computational approaches. *J. Chem. Phys.* **152**, 144703 (2020).
29. Cherstiouk, O. V. et al. Microstructure effects on the electrochemical corrosion of carbon materials and carbon-supported Pt catalysts. *Electrochim. Acta* **55**, 8453–8460 (2010).
30. Sigal, C. T. & Vayenas, C. G. Ammonia oxidation to nitric oxide in a solid electrolyte fuel cell. *Solid State Ion.* **5**, 567–570 (1981).
31. Zeng, Y. et al. Tuning the thermal activation atmosphere breaks the activity–stability trade-off of Fe–N–C oxygen reduction fuel cell catalysts. *Nat. Catal.* **6**, 1215–1227 (2023).
32. Kresse, G. & Hafner, J. Ab initio molecular dynamics for open-shell transition metals. *Phys. Rev. B* **48**, 13115–13118 (1993).
33. Kresse, G. & Hafner, J. Ab initio molecular-dynamics simulation of the liquid-metal–amorphous-semiconductor transition in germanium. *Phys. Rev. B* **49**, 14251–14269 (1994).
34. Kresse, G. & Furthmüller, J. Efficiency of ab-initio total energy calculations for metals and semiconductors using a plane-wave basis set. *Comput. Mater. Sci.* **6**, 15–50 (1996).
35. Wellendorff, J. et al. Density functionals for surface science: exchange-correlation model development with Bayesian error estimation. *Phys. Rev. B* **85**, 235149 (2012).
36. López-Urías, F. et al. Understanding the electrochemistry of armchair graphene nanoribbons containing nitrogen and oxygen functional groups: DFT calculations. *Phys. Chem. Chem. Phys.* **22**, 4533–4543 (2020).
37. Calle-Vallejo, F., Huang, M., Henry, J. B., Koper, M. T. M. & Bandarenka, A. S. Theoretical design and experimental implementation of Ag/Au electrodes for the electrochemical reduction of nitrate. *Phys. Chem. Chem. Phys.* **15**, 3196–3202 (2013).
38. Kresse, G. & Furthmüller, J. Efficient iterative schemes for ab initio total-energy calculations using a plane-wave basis set. *Phys. Rev. B* **54**, 11169–11186 (1996).
39. Wellendorff, J. et al. A benchmark database for adsorption bond energies to transition metal surfaces and comparison to selected DFT functionals. *Surf. Sci.* **640**, 36–44 (2015).

40. Shin, H., Hansen, K. U. & Jiao, F. Techno-economic assessment of low-temperature carbon dioxide electrolysis. *Nat. Sustain.* **4**, 911–919 (2021).
41. Crandall, B. S., Brix, T., Weber, R. S. & Jiao, F. Techno-economic assessment of green H₂ carrier supply chains. *Energy Fuels* **37**, 1441–1450 (2023).
42. *Final Background Document for Nitric Acid Section 8.8* (US Environmental Protection Agency, 2020); https://www.epa.gov/sites/default/files/2020-09/documents/final_background_document_for_nitric_acid_section_8.8.pdf
43. Thiemann, M., Scheibler, E. & Wiegand, K. W. in *Ullmann's Encyclopedia of Industrial Chemistry* (eds Ley, C. et al.) (Wiley-VCH, 2012).

Acknowledgements

A.L., B.S.C. and F.J. thank Washington University in St Louis for financial support. S.S. and S.D. acknowledge support from the University of Calgary's Canada First Research Excellence Fund Program, the Global Research Initiative in Sustainable Low Carbon Unconventional Resources. This research was enabled in part by the support provided by Computational Resources at the University of Calgary and Compute Canada.

Author contributions

R.X. conceived the idea, designed the experiments and prepared the manuscript. S.D. and T.J.G. performed the DFT calculations. R.X., A.L., B.H. and A.R. conducted the product analysis and catalyst characterizations. B.S.C. helped with the separation analysis. J.L. and G.W. provided the Fe–N–C catalysts. S.S. supervised the computational modelling efforts. F.J. supervised the project. All authors commented on the final version of the paper.

Competing interests

The authors declare no competing interests.

Additional information

Supplementary information The online version contains supplementary material available at <https://doi.org/10.1038/s41929-025-01315-8>.

Correspondence and requests for materials should be addressed to Samira Siahrostami or Feng Jiao.

Peer review information *Nature Catalysis* thanks Mahinder Ramdin and the other, anonymous, reviewer(s) for their contribution to the peer review of this work.

Reprints and permissions information is available at www.nature.com/reprints.

Publisher's note Springer Nature remains neutral with regard to jurisdictional claims in published maps and institutional affiliations.

Springer Nature or its licensor (e.g. a society or other partner) holds exclusive rights to this article under a publishing agreement with the author(s) or other rightsholder(s); author self-archiving of the accepted manuscript version of this article is solely governed by the terms of such publishing agreement and applicable law.

© The Author(s), under exclusive licence to Springer Nature Limited 2025